

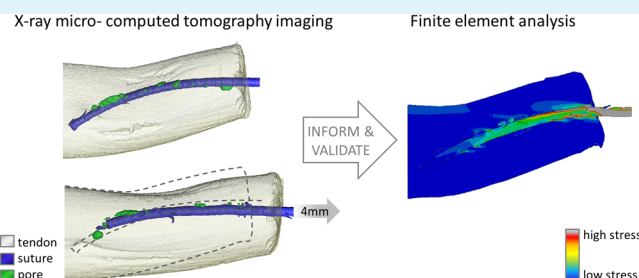
Four-Dimensional Imaging of Soft Tissue and Implanted Biomaterial Mechanics: A Barbed Suture Case Study for Tendon Repair

Shelley D. Rawson,[†] Tom Shearer,^{†,‡} Tristan Lowe,[†] Marie O'Brien,[†] Jason K. F. Wong,[§] Lee Margetts,^{||} and Sarah H. Cartmell^{*,†}

[†]School of Materials, [‡]School of Mathematics, [§]Plastic Surgery Research, and ^{||}School of Mechanical, Aerospace and Civil Engineering, University of Manchester, Oxford Road, M13 9PL Manchester, U.K.

ABSTRACT: Timely, recent developments in X-ray micro-computed tomography ($X\mu$ CT) imaging such as increased resolution and improved sample preparation enable non-destructive time-lapse imaging of polymeric biomaterials when implanted in soft tissue, which we demonstrate herein. Imaging the full three-dimensional (3D) structure of an implanted biomaterial provides new opportunities to assess the micromechanics of the interface between the implant and tissues and how this changes over time as force is applied in load-bearing musculoskeletal applications. In this paper, we present a case study demonstrating *in situ* $X\mu$ CT and finite element analysis, using a dynamically loaded barbed suture repair for its novel use in tendon tissue. The aim of this study was to identify the distribution of stress in the suture and tendon as load is applied. The data gained demonstrate a clear 3D visualization of microscale features in both the tissue and implant in wet conditions. $X\mu$ CT imaging has revealed, for the first time, pores around the suture, preventing full engagement of all the barbs with the tendon tissue. Subsequent finite element analysis reveals the localized stress and strain, which are not evenly distributed along the suture, or throughout the tissue. This case study demonstrates for the first time a powerful *in situ* mechanical imaging tool, which could be readily adapted by other laboratories to interrogate and optimize the interface between the implanted biomaterials and the soft tissue.

KEYWORDS: suture, biomaterial, tendon, tissue engineering, tomography, medical devices



1. INTRODUCTION

Assessing new implantable medical devices in preclinical models is a resource-heavy necessity which would benefit from advanced validation tools. The advancement of novel medical treatments necessitates the development of improved means with which to interrogate the new therapeutic devices and technologies. Recent developments across several areas of imaging such as X-ray microcomputed tomography ($X\mu$ CT) have culminated in the timely ability to allow four-dimensional (4D) imaging of soft tissue deformation. Three-dimensional (3D) studies of soft tissue can be achieved by confocal microscopy, serial sectioning, or serial block-face imaging; however, these methods are limited by a small field of view, can be technically challenging, and can introduce imaging artifacts. Furthermore, serial sectioning and block-face imaging are destructive, preventing the progressive application of force over time within the same sample.¹ The 4D $X\mu$ CT studies of implanted devices in an aqueous environment permit the validation of finite element (FE) modeling from which further prototypes may be developed *in silico*. Acquiring validated soft tissue mechanics via $X\mu$ CT and *in silico* modeling permits a faster and more cost-effective approach toward product development.

To enable soft tissue $X\mu$ CT imaging, previous literature has described sample staining using osmium tetroxide as a contrast

agent,² and other less toxic stains have since been described, making sample staining more routine.³ Although these stains offer good tissue contrast, their effects on soft tissue mechanics limit their use to static imaging. Phase contrast imaging improves the visibility of edges between features of similar X-ray attenuation and has been exploited on synchrotron systems for biological imaging since the mid-90's⁴ and is now attainable using laboratory X-ray sources,⁵ making this technology more accessible. Phase contrast does not affect soft tissue mechanics; however, the blurring of edges can make their exact position ambiguous, and imaging remains difficult at the boundaries between materials of very similar X-ray attenuation such as water and tendon. $X\mu$ CT can now be performed at spatial resolutions of <50 nm,⁶ and when used in tandem with traditional techniques such as histology, energy-dispersive X-ray spectrometry, scanning electron microscopy, or transmission electron microscopy, a wealth of 3D structural and compositional data can be obtained.⁷ This is furthered by the potential of using $X\mu$ CT to inform FE modeling, obtaining quantitative stress and strain data, which is becoming commonplace in osteoporotic bone density and strength

Received: June 11, 2018

Accepted: October 22, 2018

Published: October 22, 2018

studies^{8,9} and can be validated using time-lapse tomography.¹⁰ These advancements have culminated in the timely potential to concurrently interrogate the morphology, composition, and mechanical response of soft tissue implants *in situ* using multimodal techniques which we describe herein. It is with this recent advancement in CT resolution and contrast agent development that this case study has been performed to demonstrate the capability in the biomaterial arena.

Biomaterials for tissue engineering (TE) has become a diverse field seeking to mimic, grow, and regenerate all tissues and organs of the body. The biomaterials for tissue scaffolds exhibit a diverse range of morphologies, but typically having nanoscale features, produced by electrospinning, hot embossing, or soft lithography, for example, within a construct with dimensions typically on the centimeter length scale.^{11,12} The macro- and micromechanical environment of a given biomaterial *in situ* is becoming increasingly important. An implant must withstand mechanical forces throughout the lifetime of the device, which is particularly poignant in load-bearing applications such as muscle, tendon, abdominal wall, and skin. The implant may be required to transfer the mechanical forces to the regenerating tissues in the case of degradable devices or to maintain mechanical integrity for many years in the case of nondegradable devices. In cellularized scaffolds, localized mechanical forces can influence cell homeostasis, signaling, differentiation, and lineage.¹³ An implantable device is subject to a challenging environment, affected by chemical, biological, and mechanical damage, making prediction of this multifactorial environment challenging. *In silico* modeling is therefore a vital development in designing reliable devices with a predictable *in situ* life span.¹³ For FE modeling, the 3D geometry of the implant and the surrounding environment must first be defined. This paper presents the novel combination of tailored sample preparation, *in situ* mechanical testing, and X μ CT to both inform and validate FE analysis. The paper demonstrates this workflow using the case study of an incrementally loaded tendon with an implanted barbed suture made of a degradable polymeric biomaterial. This CT image-validated FE technique offers important localized stress distribution data sets on a loaded polymeric medical device implanted within soft tissues in an aqueous environment.

1.1. Case Study: Barbed Suture Tendon Repair. We have selected the example of a sutured hand tendon repair, as there is a clinical need for improved techniques within this field. Over 50 000 people are treated in the UK per annum for tendon injuries,¹⁴ over two-thirds of which are hand tendon injuries.¹⁵ Zone 2 flexor tendon rupture poses a particular challenge as the tendon must glide through the flexor sheath within this region to enable flexion of the digit. Typical repairs involve reapproximating the severed ends using surgical sutures, which was described in 1918 by Bunnell *et al.*¹⁶ Over the decades, improvements have been made to the suture arrangement, to increase the strength of the repair and to minimize the formation of scar tissue (known as adhesions) which restricts tendon glide. In recent years, X-ray radiography has enabled a detailed interrogation of failure in tendon suture arrangements.¹⁷ Many intricate suture arrangements can now be found in the literature, which have been reviewed in detail.¹⁸ Nevertheless, the procedure remains largely unchanged from that which was performed a century ago; severed tendon ends are still rejoined by nondegradable surgical sutures. In recent years, several research groups

internationally are investigating novel methods of tendon repair to improve prognoses, one of which is barbed suture repair.¹⁹ The research into barbed suture for tendon repair is still in its infancy.

Barbed suture is said to distribute load evenly throughout the suture strand and tissue via periodic microscale barbs on its surface, providing superior tissue anchorage over conventional sutures.²⁰ Although typically used in low load-bearing tissues, barbed sutures are now being considered for high load-bearing applications such as tendon repair.²¹ Their use may address the uneven stress distribution within conventionally sutured tendons,²² which is thought to incite acellular regions, observed within hours and persisting for at least 1 year postoperatively.²³ A successful barbed tendon repair has the potential to benefit the 25% of flexor tendon repair patients whom attain poor mobility after 6 months postoperatively.²⁴ Unfortunately, however, published data to support the claims of evenly distributed stress from barbed suture are lacking. If barbed attachment is to be pursued for use in high load-bearing applications such as tendon repair, the load-bearing characteristics must be assessed to consider how the barbs fail when overloaded and how stress distributions may affect the healing environment of the tissue. Strength must be maintained during the initial 8 weeks of active mobilization rehabilitation,²⁵ after which sufficient collagen will have been replaced for normal activity to be resumed.²⁶ In the case of degradable devices, the rate of degradation must allow necessary time for tissue healing.

Stress distribution within a tendon repair can be revealed using FE analysis.²² Ingle *et al.* performed FE analysis of individual suture barbs, considering how barb geometry can be tailored to attach to skin or tendon.²⁷ The results showed that the ideal barb for skin attachment was different to the ideal geometry for tendon attachment. Furthermore, Ingle *et al.* concluded that the barbs fail by two mechanisms—bending or peeling from the suture shaft;²⁷ however, this study only considered stress distribution in individual barbs, rather than multiple barbs along a length of suture, and the study used an idealized geometry of the tendon and suture. Failure by bending or peeling may be, in part, due to the manufacturing technique of the suture used by Ingle and King, whereby cuts were made in the suture to produce the barbs.²⁸

FE analysis can offer information on stress and deformation arising within an implanted device under force application; however, *in silico* modeling requires validation from experimental data. An FE model can be generated from X μ CT data, providing a detailed 3D geometry and enabling an accurate validation against experimental results of sample deformation; however, X μ CT poses significant challenges with respect to the imaging of polymeric biomaterials *in situ* within soft tissues. Sample hydration is a concern, as X μ CT imaging typically takes several hours. The X-ray attenuation of a soft tissue and polymeric implant and Good's buffer (a salt-balanced solution to maintain sample hydration) is very similar; thus, a poor contrast would be achieved and the different structures would not be identifiable.³ Heavy metal staining provides good X-ray contrast, allowing the discernment between different soft tissues, as demonstrated in a range of samples including embryos,^{2,3} brain,²⁹ and collagen-based TE scaffolds.³⁰ Iodine potassium iodide (I₂KI) is reported to provide a good contrast in tendon, allowing observations of fascicles which form a part of the tendon hierarchical structure.³² Staining does however cause tissue shrinkage,

exacerbated by a longer staining duration or a higher concentration staining solution.³³ Tissue fixation is commonplace and intends to minimize the tissue shrinkage caused by staining; however, fixation affects the mechanical properties because of the cross-linking of the tissue,³⁴ which would affect the interaction between barbs and tendon, impacting on the results of tensile testing. Here, we describe tendon surface staining without prior fixation, using a customized iodine stain designed to minimize the change in mechanical properties and tissue morphology.

This study is the first to perform 4D $X\mu$ CT imaging of an implanted biomaterial in soft tissue during in situ loading in an aqueous environment. The customized staining method developed for this case study has permitted $X\mu$ CT observation of a sutured tendon sample in the relaxed position and subsequent $X\mu$ CT imaging of the same sample following suture withdrawal. The $X\mu$ CT-informed FE analysis has provided details of local stresses and of tissue and biomaterial deformation. Feedback from the FE model allows validation against the $X\mu$ CT sample deformation data. Through the combination of these techniques, we have investigated the viability of a novel soft tissue attachment method by identifying the deformation and stress distribution. The methods described can be readily adapted for the study of polymeric implants within soft tissues to provide 3D qualitative morphological and stress–strain data.

2. MATERIALS AND METHODS

2.1. Tendon Samples. Porcine fore-trotter *flexor digitorum profundus* (FDP) tendon is a suitable surrogate for human FDP. This is based on the robust study by Havulinna et al., who conducted ex vivo tensile testing of sutured human cadaver FDP and porcine FDP from the central two digits, demonstrating no significant difference in failure force between the two groups.³⁵ Porcine fore-trotters from 12 months old pigs were sourced from a local abattoir (Staffordshire Meat Packers Ltd., Stoke-on-Trent) less than 24 h after slaughter. The FDP tendons from the central two digits of the trotters were excised (thus, two tendon samples were obtained from each trotter), and the central portion of the tendon was dissected down to 6 cm in length (such that the fibrocartilage regions were removed). The samples were submerged in Dulbecco's phosphate-buffered saline (without Ca^{2+} or Mg^{2+} ; PBS; PAA Laboratories, Pasching, Austria) and then immediately frozen and stored at $-20\text{ }^{\circ}\text{C}$. When required, the tendons were defrosted at room temperature (RT) and immediately prepared for testing. Although freezing reportedly reduces Young modulus of the tendon, it is required for practical purposes and is commonly performed.³¹

2.2. Staining Solutions. A conventional iodine potassium iodide solution ($\text{I}_2\text{KI}-\text{dH}_2\text{O}$) was prepared as previously described;³² 0.1% iodine metal and 0.2% potassium iodide were dissolved in distilled water at RT. I_2KI in Dulbecco's PBS (without Ca^{2+} or Mg^{2+} , PAA Laboratories, Pasching, Austria; $\text{I}_2\text{KI}-\text{PBS}$) was prepared by dissolving the same proportions of iodine metal and potassium iodide in PBS at RT.

2.3. Staining Time Course Study. A 6 cm length section of tendon was incubated in $\text{I}_2\text{KI}-\text{PBS}$ at $4\text{ }^{\circ}\text{C}$ with gentle tilting and rotation. At 2, 4, 6, 8, 24, and 48 h, a 2 mm length of tendon was cut from the end using a scalpel and discarded; then, a 5 mm length of tendon was cut and frozen at $-20\text{ }^{\circ}\text{C}$ in PBS until all time-point samples were harvested. The samples were then defrosted at RT and stacked vertically within a 1.5 mL Eppendorf, secured together using a cyanoacrylate adhesive (Loctite, Düsseldorf, Germany), and then submerged in PBS before immediate $X\mu$ CT scanning. This arrangement was to permit simultaneous $X\mu$ CT scanning of all samples on a single scan.

Scanning was performed using the Nikon-customized bay in the Manchester X-ray Imaging Facility, University of Manchester, which

houses a Nikon Metris 225/320 kV system and employs a $2\text{K} \times 2\text{K}$ PerkinElmer 1621-16-bit amorphous silicon flat-panel detector with a $200\text{ }\mu\text{m}$ pixel pitch (Nikon, Tokyo, Japan). Scanning was performed at a voltage of 60 kV and current of $175\text{ }\mu\text{A}$ using a tungsten target. The source-to-sample and source-to-detector distances were 180.6 and 1400.2 mm, respectively, giving a voxel size of $15.4\text{ }\mu\text{m}$. The exposure time per projection was 1451 ms, and a total of 2001 projections were taken through 360° of rotation.

Following acquisition, the data were reconstructed using a Nikon Metris CTPPro (Metris XT 1.6, version 2.1; Tokyo, Japan), with no beam-hardening correction. The data were imported into Avizo (Version 7.0; Visualization Sciences Group, Bordeaux, France), and a non-local means filter was applied using default settings to remove noise from the data set. A virtual section from the center of each time-point sample was exported as a .jpg for analysis using ImageJ (version for Windows, open source software, available at <http://rsb.info.nih.gov/ij/download.html>). A 20 pixel thick line was drawn across each tendon cross section, intersecting the tendon center, and gray scale values were obtained along the line (averaged over its 20 pixel thickness) and plotted against the distance through the sample.

2.4. Observing Stained Tendon Morphology. The tendon samples were stained in $\text{I}_2\text{KI}-\text{dH}_2\text{O}$ or $\text{I}_2\text{KI}-\text{PBS}$ for 24 h at $4\text{ }^{\circ}\text{C}$ with gentle tilting and rotation (six replicates in each group). Two control groups were also prepared: one was incubated in PBS for 24 h at $4\text{ }^{\circ}\text{C}$ with gentle tilting and rotation, and the other group was prepared for cryosectioning immediately, with no incubation (six replicates in each control group). Ahead of cryosectioning, a 1 cm length of tendon was removed from the approximate center of each sample using a scalpel. The 1 cm tendon samples were embedded longitudinally in an optimal cutting temperature compound (OCT; Fisher Scientific, Loughborough, UK) and immediately frozen using liquid nitrogen. The samples were then sectioned using a cryostat (CM3050S; Leica Biosystems, Newcastle upon Tyne, UK) at $-20\text{ }^{\circ}\text{C}$ at a thickness of $50\text{ }\mu\text{m}$. The samples were rinsed in water to remove any excess OCT. The control samples were then stained with hematoxylin and eosin to reveal tissue morphology (Fisher Scientific, Loughborough, UK). All sections were coverslipped and then imaged using a light microscope (DMRB; Leica Biosystems, Newcastle upon Tyne, UK). It should be noted that the $\text{I}_2\text{KI}-\text{dH}_2\text{O}$ and $\text{I}_2\text{KI}-\text{PBS}$ sample groups have not been histologically stained.

2.5. Establishing the Tangential Modulus of Stained Tendons. Tendon samples, 6 cm in length, were stained in $\text{I}_2\text{KI}-\text{dH}_2\text{O}$ or $\text{I}_2\text{KI}-\text{PBS}$ for 24 h at $4\text{ }^{\circ}\text{C}$ with gentle tilting and rotation or left unstained as a control (eight replicates in each group). The unstained controls were tested immediately with no PBS incubation. [Preliminary data have demonstrated no significant difference in the tendon tangential modulus when comparing no incubation with 24 h PBS incubation (data not shown)].

The tendon width (h) and thickness (t) were measured at the tendon center, and 1 cm either side, using digital vernier calipers, and the mean cross-sectional area (A) was calculated for each tendon using the equation of an ellipse ($A = \pi ht/4$).

Tensile testing was performed using an Instron 3344 load frame (Instron, High Wycombe, UK) and a 2 kN load cell. The Instron wedge action grips (Instron, High Wycombe, UK) were positioned in the load frame at a grip-to-grip distance of 2 cm. The gripping surface was enhanced using a 120 grit silicon carbide waterproof electro-coated sandpaper (Asia Abrasives, Quezon City, Philippines) attached using a double-sided paper tape (RS, Corby, UK). The tendon samples were tightened into the grips, a 0.1 N pretension was applied, and the samples were then tested to failure in air at 0.5 mm s^{-1} . This is equivalent to a strain rate of $2.5\% \text{ s}^{-1}$. Force and displacement were recorded at a sampling rate of 20 Hz. Tangential modulus was obtained from the approximately linear region of the stress–strain curve before calculation of the mean. The data were statistically analyzed using analysis of variance, with a post hoc least significance difference test, using SPSS (version number 22) software. The data are presented as mean \pm SD, and a p value less than 0.05 was considered to be significant.

2.6. Effects of Staining on Barb Attachment. Size 2 polydioxanone (PDO) barbed suture (Quill PDO-2; Angiotech Pharmaceuticals, Vancouver, Canada) was used throughout this study. This suture possesses unidirectional barbs, helically arranged around a monofilament PDO suture. The suture was stained for 24 h in I_2KI-dH_2O at RT or left unstained as a control. A transverse cut was made in the center of each tendon, and the distal end was discarded. The suture was inserted 10 mm into the tendon from the freshly cut end, exiting through the epitenon (four replicates in each group). The excess suture was cut flush with the tendon surface.

Tensile testing was performed using an Instron 3344 load frame (Instron, High Wycombe, UK) and a 100 N load cell. A Bose self-tightening tissue grip and a Bose-sandblasted tissue grip (Part of the Bose BioDynamic 5110 ElectroForce Instrument; Bose Corporation, Eden Prairie, Minnesota, USA) were attached to the top and bottom of the load frame, respectively, using custom-made adapters, and a PBS-filled tank was positioned such that the whole sample would be submerged. The tendon was attached to the top grip, and the suture was attached to the bottom grip. No pretension was applied because of the low expected failure load, to ensure acquisition of the full loading curve. Instead, this was accounted for during analysis by taking 0.1 N as the start point of the test (thus, a 0.1 N preload was retrospectively applied). The samples were tested to failure at a displacement rate of 0.5 mm s^{-1} . Force and displacement were recorded at a sampling rate of 20 Hz. The maximum recorded force was taken as the failure force. The mean failure force of each experimental group was calculated. Significance was determined using the Student *t* test, and *p* values ≤ 0.05 were considered significant.

2.7. $X\mu$ CT Scans of Sutured Tendons. A transverse cut was made in the center of the excised tendon sample, and the distal end was discarded. The tendon was incubated in I_2KI -PBS for 24 h at 4°C . Meanwhile, a Quill PDO-2 barbed suture was incubated in I_2KI - dH_2O for 24 h at RT. The suture was inserted 10 mm into the tendon from the freshly cut end, exiting through the epitenon. The excess suture was cut flush with the tendon surface. The sample was inserted into a custom-made tensioning apparatus, which applies tension to the sample via rotation of a nut that withdraws a threaded shaft (Figure 1). The apparatus permits submersion of the sample throughout

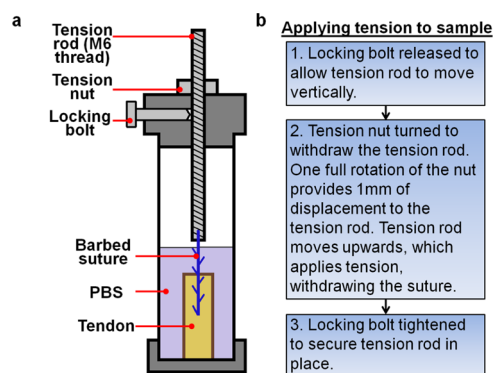


Figure 1. (a) Schematic detailing the tension rig apparatus and (b) flow diagram detailing how tension is applied to the sample using the rig.

testing to maintain hydration. The tendon end was secured in position using a cyanoacrylate adhesive (Loctite, Düsseldorf, Germany), and the suture end was secured in position using a rapid-drying epoxy adhesive (Bostik, Milwaukee, Wisconsin, US). After 5 min of drying time, PBS was added to submerge the tendon.

Two samples were prepared: sample 1 for the large displacement and sample 2 for the small displacement $X\mu$ CT scan. Scanning was performed using the equipment and settings described in Section 2.3 with the following exceptions. For the large displacement study (sample 1), the source-to-sample and source-to-detector distances were 71.5 and 1407.0 mm, respectively, giving a voxel size of $10.2 \mu\text{m}$. For the small displacement study (sample 2), the source-to-sample

and source-to-detector distances were 71.0 and 1400.2 mm, respectively, giving a voxel size of $10.0 \mu\text{m}$. After the initial scan with the sample in the relaxed position, tension was applied to withdraw the suture, and a subsequent scan was performed. A 15 min delay was imposed between the application of tension and the start of the next scan to allow for tissue relaxation and thus prevent sample movement during scanning which would otherwise compromise the $X\mu$ CT scan (15 min was determined sufficient in preliminary stress relaxation experiments; data not shown). The large displacement sample was scanned at 0, 2, and 4 mm suture withdrawal. The small displacement sample was scanned at 0 and 0.5 mm suture withdrawal. The large and small displacement increments were selected to observe barb bending up until failure and for the validation of the FE model, respectively.

The data were reconstructed using a Nikon Metris CTPro (Metris XT 1.6, version 2.1; Tokyo, Japan), with no beam-hardening correction. The data were imported into Avizo (Version 7.0; Visualization Sciences Group, Bordeaux, France), and the non-local means filter was applied with default settings and segmentation was then performed manually. The data were resampled, resulting in the voxel sizes of 40.8 and $40.0 \mu\text{m}$ for the large and small displacement samples, respectively, and the surfaces were generated. The length and angle of each barb were measured from each scan. Barb length was measured as the chord from the root of the barb to the tip of the barb (chord R-T; Figure 2b). A second chord was drawn from the root of

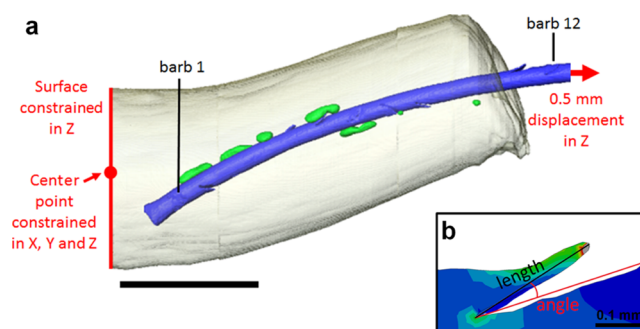


Figure 2. (a) $X\mu$ CT-informed FE model, showing segmented data from the small displacement study (sample 2) in the unloaded position (used to inform the FE model geometry) and the boundary conditions applied to the FE model, noted in red (gray = tendon, blue = suture, green = air-filled pores. Scale bar = 4 mm). (b) Illustration showing the measurement of barb length and angle from FE results. (The same method was used for the barb measurements of CT data.)

the barb to the tip of the barb cut-line on the suture shaft (chord R-C). The barb angle was measured as the angle between the chord R-T and chord R-C (Figure 2b).

2.8. FE Analysis: Small Displacement Study. The segmented data from the small displacement study (sample 2) scanned in the 0 mm suture withdrawal position were exported from Avizo as a stack of .tiff images and imported into ScanIP (Simpleware, Exeter, UK). Following a mesh convergence study (data not shown), the full data set was downsampled to 30% of the original scan, which was required to produce a mesh of suitable compromise between accuracy and computational cost. All contact pairs were added between the tendon and suture, and then a mesh of 10-node tetrahedral (Abaqus code: C3D10) elements was produced and exported from ScanIP as an Abaqus input file (version 6.14-2; Simulia, Providence, Rhode Island, USA). Two Abaqus meshes were produced via this method, one with and one without air-filled pores (containing 331 659 and 303 088 elements, respectively), which were observed within the tendon during the $X\mu$ CT scans (Section 3.2).

Following the data import into Abaqus, the tendon was described as transversely isotropic linear elastic using the engineering constants obtained from the homogenization of a tendon microstructure model where the fibril modulus was 1600 MPa, matrix modulus was 1 MPa,

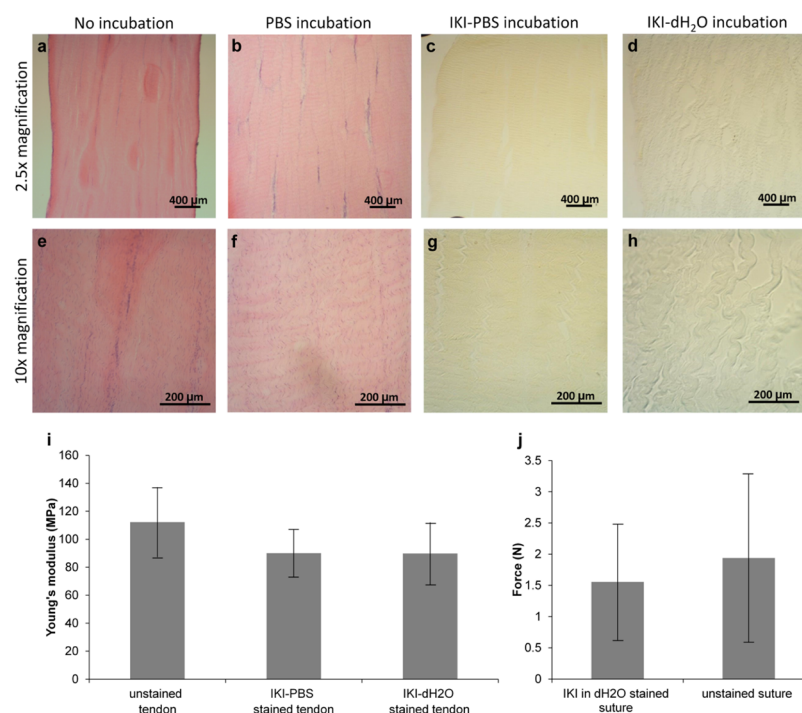


Figure 3. Effects of tendon and suture staining. (a–h) Tendon longitudinal sections ($n = 6$) at $50\ \mu\text{m}$ thickness after undergoing the following treatments: immediately excised control samples with no incubation in solution (a,e), 24 h incubation at $4\ ^\circ\text{C}$ in PBS, (b,f) 24 h incubation at $4\ ^\circ\text{C}$ in IKI–PBS (c,g), and 24 h incubation in IKI– dH_2O (d,h). [(a–d) 2.5 \times magnification, (e–h) 10 \times magnification]. (i) Young's modulus of unstained (with no PBS incubation), unstained following 24 h incubation in PBS at $4\ ^\circ\text{C}$, I_2KI –PBS stained (24 h incubation at $4\ ^\circ\text{C}$), and I_2KI – dH_2O stained (24 h incubation at $4\ ^\circ\text{C}$) tendons ($n = 8$, error bars show standard deviation). (j) Failure force of tendons sutured with I_2KI – dH_2O stained and unstained barbed sutures, loaded under tension ($n = 4$, error bars show standard deviation).

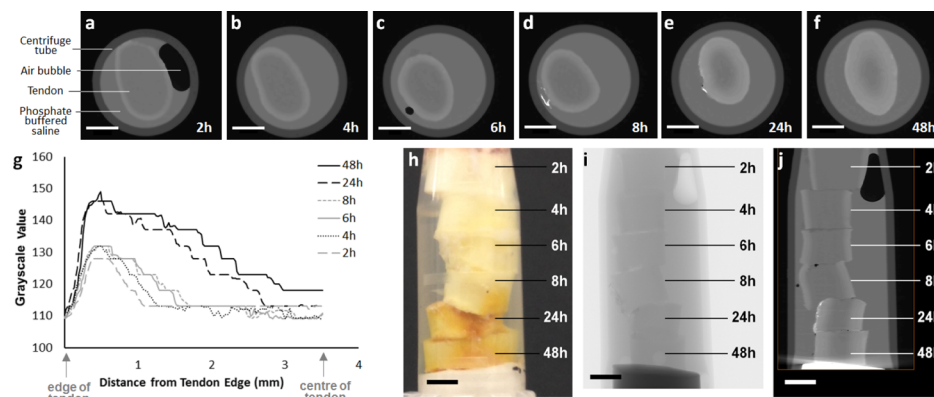


Figure 4. Optimization of the iodine-staining protocol. (a–f) Virtual sections from the reconstructed $X\mu\text{CT}$ time course study scan through the approximate center of each tendon sample following staining using I_2KI –PBS for (a) 2, (b) 4, (c) 6, (d) 8, (e) 24 h, and (f) 48 h. (g) Gray scale values from the edge to the center of the tendon, obtained from the virtual sections (average over 20 pixels). A higher gray scale value signifies greater X-ray absorbance because of more uptake of iodine. (h–j) View of the I_2KI –PBS stained tendon samples stacked in the centrifuge tube during $X\mu\text{CT}$ imaging. (h) Photograph. (i) X-ray radiograph. (j) $X\mu\text{CT}$ virtual section. (All scale bars 4 mm).

and Poisson's ratio was 0.3.²² The values of the engineering constants were as follows: Young's modulus (E) values: $E_1 = E_2 = 4.751048729\ \text{MPa}$, $E_3 = 962.99.9984\ \text{MPa}$; Poisson's ratio (ν) values: $\nu_{12} = 0.253220532$, $\nu_{13} = \nu_{23} = 0.022529523$; and Shear modulus (G) values: $G_{12} = 1.181960429\ \text{MPa}$, $G_{13} = G_{23} = 45.64068793\ \text{MPa}$ (10 significant figures are necessary to fully describe the material). The tendon orientation of anisotropy was defined such that the stiffness was greater in the direction parallel with the long axis of the tendon. The suture was described as isotropic linear elastic with Young's modulus of 1 GPa, Poisson's ratio of 0.4, and the coefficient of friction was set to 0.005 as described previously.²² Three boundary conditions were applied to withdraw the suture by 0.5 mm, to hold the tendon in position, and to prevent free body movement (Figure 2a). This

simulates the loading conditions which were employed in the 0.5 mm suture pull $X\mu\text{CT}$ scan during the small displacement study (sample 2).

Once the resultant stress and deformation were obtained from the FE analysis, the angles of the barbs were measured from the FE result of the deformed shape following 0.5 mm simulated suture withdrawal, along with the $X\mu\text{CT}$ data of sample 2 in the unloaded and 0.5 mm suture withdrawal position. These barb angle measurements were made as described in Section 2.7 and are shown in Figure 2b.

3. RESULTS

3.1. Development of the Staining Method. The uniaxial tensile testing of stained and unstained tendons

demonstrated no significant difference in Young's modulus of the tendon between the two stained sample groups and the unstained control tendon group which was tested immediately after excision (Figure 3i).

The images of the tendon sections following 24 h of staining revealed increased tissue damage from the I_2KI-dH_2O stain (Figure 3d,h), compared with the $I_2KI-PBS$ stained sample (Figure 3c,g).

No difference is observed when comparing the tissue morphology of the unincubated controls (Figure 3a,e) with those incubated in PBS for 24 h (Figure 3b,f) observed across all replicates. The characteristic crimp formation of the tendon collagen fibrils is also clearly visible in the samples incubated for 24 h in $I_2KI-PBS$ (Figure 3c,g) observed across all replicates. The samples incubated for 24 h in I_2KI-dH_2O (Figure 3d,h) present a different morphology compared with that of the unincubated control; the fibrils appear separated from each other, and the crimp appears disrupted. This was apparent in four out of the six replicates. The $I_2KI-PBS$ stain was selected for tendon staining going forward, in the interest of minimizing tissue damage, as the cryosections demonstrated that it had a lesser effect on the morphology of the tendon tissue compared with the conventional I_2KI-dH_2O stain.

The results of the suture pull-out test demonstrated no significant difference in the force required to withdraw stained and unstained sutures from the tendon (Figure 3j). This suggests that suture staining for 24 h using I_2KI-dH_2O does not significantly affect the attachment of the suture barbs to the tendon tissue. This staining protocol was therefore regarded to be suitable for subsequent $X\mu CT$ imaging of suture withdrawal.

The results of the staining time course study are illustrated in Figure 4. Similar staining penetration and intensity are observed from the 2, 4, 6, and 8 h samples (Figure 4a–d). From 8 to 24 h staining duration, there is an increase in staining intensity, resulting in higher gray scale values around the edge of the tendon in the $X\mu CT$ scan, and the staining penetration has approximately doubled from 1.5 mm at 2–8 h to 3 mm at 24–48 h (Figure 4a–f). A small increase in staining intensity and penetration is observed when comparing 24 and 48 h staining durations (Figure 4e,f). From the reconstructed virtual section of the samples, the tendon edge is clearly visible in the 2 h stained sample (Figure 4a); however, transmission is extremely low through the sample, and the tendon edge is not visible from the X-ray projection in the 2 h sample (Figure 4i). The lack of tendon visibility on the X-ray projection impairs the centering of the sample, and a larger field of view is then necessary to ensure the whole sample is in view, thus reducing the achievable resolution. As such, a 24 h staining duration was selected, as the tendon edge is clearly visible on the X-ray projection at this time-point.

3.2. $X\mu CT$ Scans: Large Displacement Study at 0, 2, and 4 mm Suture Withdrawal. The $X\mu CT$ volumes from the large displacement study (sample 1) were reconstructed successfully, and the segmented data are displayed in Figure 5d–f. Upon withdrawal of the suture by an initial 2 mm, the sample is first seen to straighten out (Figure 5d,e), whereas the suture remains in position within the tendon. When 4 mm suture withdrawal is reached, the suture can be seen to have displaced from its original position within the tendon, and barb bending is observed (Figure 5e,f, black arrow).

The data obtained during staining optimization show the force–displacement curves as the barbed suture is withdrawn

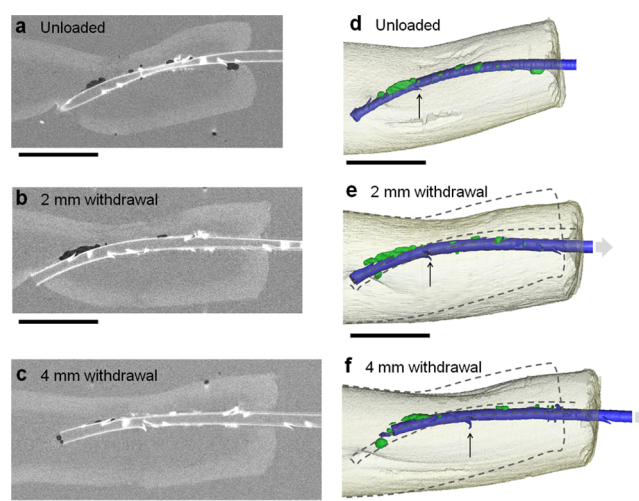


Figure 5. Large displacement study (sample 1) $X\mu CT$, unfiltered, virtual sections (a–c), and segmented data (d–f). (a,d) 0 mm suture withdrawal (unloaded), (b,e) 2 mm suture withdrawal, and (c,f) 4 mm suture withdrawal. (Figures a–c: white = iodine-stained tendon outline, pale gray = iodine-stained tendon outline, dark gray = unstained regions within the tendon/suture, and PBS surrounding the sample, black = air). (Figures d–f: pale gray = tendon, blue = suture, green = air-filled pores, gray arrow = direction of suture pull, black arrow = barb number 4 exhibiting bending, gray dotted outline = unloaded position of the suture and tendon, superimposed over figures e and f). All scale bars = 4 mm.

from the tendon (Figure 6). All the four samples withstood suture displacement of at least 4 mm before failure, providing

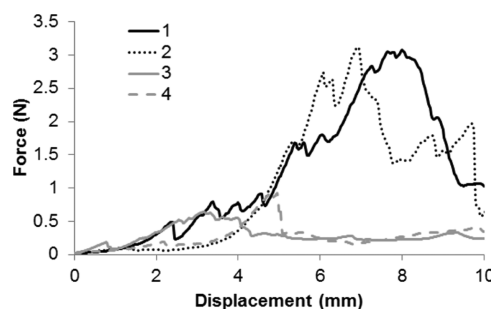


Figure 6. Force–displacement data obtained during suture pull-out testing of tendon samples sutured with I_2KI-dH_2O stained barbed suture.

confidence that the suture pull-out positions of 2 and 4 mm observed during the $X\mu CT$ study are likely to be prior to barbed suture attachment failure.

Air-filled pores were identified within the tendon (Figure 5a–c), recognized as air, as they had the same gray scale value as the other areas of the scan known to be regions of air. The air pores within the tendon were only located adjacent to the suture strand.

The analysis of the barb angles as the suture is withdrawn demonstrated that only two barbs were continually increasing in angle throughout the suture withdrawal (Figure 7a). Five barbs present an initial angle increase from 0 to 2 mm suture withdrawal followed by a decrease in angle from 2 to 4 mm withdrawal (Figure 7b). Four barbs display the opposite profile, initially reducing in angle, followed by an increase (Figure 7c). One barb continually decreases in angle

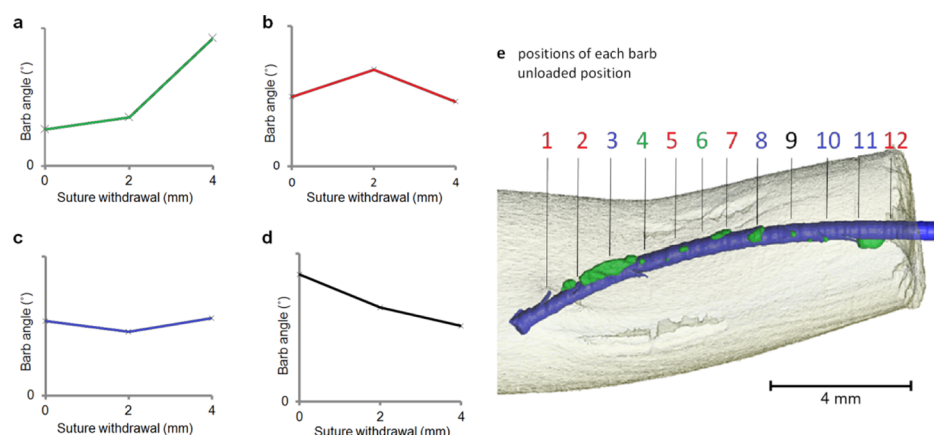


Figure 7. Barb-bending profiles during suture withdrawal, observed during the large displacement study (sample 1). (a) Increasing barb angle throughout, observed in barbs 4 and 6. (b) Initial increase, followed by a decrease in angle, observed in barbs 1, 2, 5, 7, and 12. (c) Initial decrease, followed by an increase in angle, observed in barbs 3, 8, 10, and 11. (d) Decreasing barb angle throughout, observed in barb 9. (e) Location of each barb within the tendon, shown on the unloaded sample position.

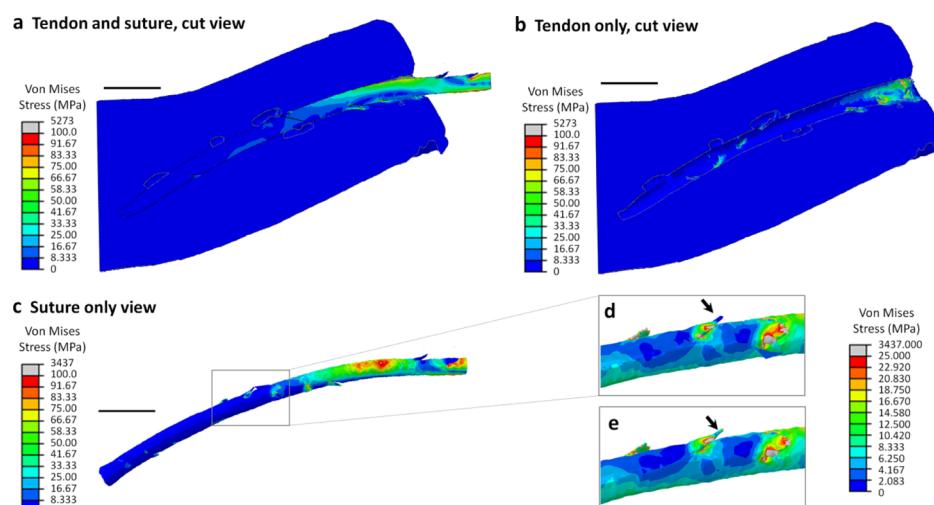


Figure 8. FE model results, simulating a 0.5 mm suture withdrawal. (a) Cut view through the center of the tendon and suture (from the simulation which includes pores). (b) Cut view through the center of the tendon, showing the tendon alone, with the stress contour plot limits adjusted to more clearly show the tendon stresses (from the simulation which includes pores). (c–e) View of the suture alone, with the stress contour plot limits adjusted to more clearly show the suture stresses. (d) View of barb number 7 (black arrow) which lies within a pore, from the FE simulation which includes the pores. Note that low stress is seen at the barb tip (indicated by the dark blue color). (e) View of barb number 7 (black arrow) from the FE simulation which omits the air-filled pores. Note that moderate stress is seen at the barb tip (indicated by the green color). (All scale bars 2 mm).

throughout the suture withdrawal (Figure 7d). No correlation is observed between the location of the barbs and their bending profile. No significant difference in barb length was observed as the suture was withdrawn, demonstrating that none of the barbs peeled from the suture shaft.

3.3. $X\mu$ CT Scans and Subsequent FE Analysis: Small Displacement Study at 0 and 0.5 mm Suture Withdrawal. The scanned volumes from the small displacement study (sample 2) were reconstructed and segmented successfully. The unloaded position $X\mu$ CT scan was converted into an FE mesh (as described in Section 2.8), and the results of a 0.5 mm suture pull FE simulation are shown in Figure 8. The mean barb angle of the 12 barbs within the tendon in the 0 mm $X\mu$ CT scan, the 0.5 mm suture withdrawal $X\mu$ CT scan, and the 0.5 mm suture withdrawal FE simulation results were $15.1^\circ (\pm 2.6^\circ)$, $22.0^\circ (\pm 5.4^\circ)$, and $18.9^\circ (\pm 5.7^\circ)$, respectively (Figure 9).

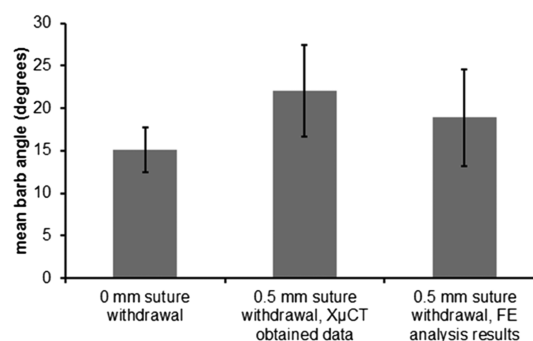


Figure 9. Mean barb angle measurements of the small displacement sample (sample 2), comparing the barb positions from the 0 and 0.5 mm displacement $X\mu$ CT scans, and the 0.5 mm displacement FE results. (Error bars are standard deviations).

The FE data highlight that stress is not evenly distributed throughout the tendon tissue. Instead, low stress is observed throughout the majority of the tendon tissue, with high stress regions concentrated close to the suture barbs. The highest stress is concentrated at the root of the suture barbs, and in particular, around the barbs closest to the cut end of the tendon. With respect to the suture, although all barbs do exhibit some level of stress, suggesting an engagement between the barb and the tendon, stress is not evenly distributed throughout the strand. The greatest suture stress is observed toward the cut end of the tendon.

Figure 8c–e shows the stress distribution from the FE results in the suture alone. Low stress is observed at the tip of barb 7 (Figure 8d), which is embedded within an air-filled pore; however, other barbs embedded within the tendon exhibit moderate to high stress at the tip. After the FE analysis was repeated with the air-filled pores omitted from the model, barb 7 exhibited moderate stress at the tip (Figure 8e). This demonstrates that the presence of the air-filled pores impairs effective attachment between the barbs and tissue.

4. DISCUSSION

Through this case study, we have demonstrated the effective sample preparation and time-lapse $X\mu$ CT imaging of a polymeric biomaterial implanted within soft tissues to inform and validate an FE model. The sample preparation successfully enabled reliable reconstruction of the $X\mu$ CT data with sufficient contrast to allow 3D visualization of the tendon and embedded barbed suture. The FE model could then be informed and validated by $X\mu$ CT data. In silico modeling offers a means of redesigning and optimizing a device to better withstand the unique mechanical stresses arising in a given operating environment. Although FE analysis is commonplace in the engineering field, it is in relative infancy within the medical setting. This paper makes inroads toward wider in silico modeling of mechanical stress for clinical applications. This methodology could address the need to study the in situ micro- and macromechanics of tissue repair devices, wound closure techniques, and implanted tissue constructs¹³ in a range of soft tissues including tendon, ligament, muscle, abdominal tissues, and skin.

4.1. $X\mu$ CT of Implanted Biomaterials. Enabling the time-lapse imaging of soft tissues in an aqueous environment hinges on effective sample preparation for enhanced $X\mu$ CT contrast. The predominant concerns are to maintain sample hydration during scanning and ensure that the mechanical properties and tissue morphology are not altered. These challenges have been addressed through applying a heavy metal stain without prior tissue fixation and development of a staining protocol which minimizes change in the tissue mechanical properties and morphology compared with the conventional fixing and staining protocol. For translation of this method to other materials and tissues, sample preparation will require tailoring to each given application. Staining uptake is likely to differ for different tissues and materials, and a time course study similar to that described here and elsewhere in previous literature^{36,37} is advisable. Other tissues may also present a different degree of mechanical or morphological change during the staining of the unfixed tissue; thus, it cannot be assumed that it will behave the same as the tendon in this study. Although some leaching of the stain from the tendon was observed over periods of several hours, the rate was not sufficient to adversely affect the $X\mu$ CT reconstruction following the 47 min scans.

This may be of concern for longer scanning times, and leaching rate may differ in other tissues; thus, caution is advised. This study provides a framework for validating the sample preparation method for alternative tissues and materials to ensure that the tissue is mechanically and morphologically preserved and to ensure that reliable $X\mu$ CT data can be obtained.

4.2. Sutured Tendon Case Study. Our FE data provide insights into the distribution of stress through the suture and tissue upon suture withdrawal. One of the reported benefits of barbed suture is even distribution of stress along the suture length.²⁰ Contrary to this claim, our FE findings demonstrate that stress is not evenly distributed. Barbs closest to the cut end of the tendon withstand the greatest stress, with the deepest barbs withstanding less stress (Figure 8c). Furthermore, the stress in the tissue is concentrated closest to the suture strand; very little stress is experienced throughout the majority of the tendon (Figure 8b). Uneven stress distribution presents several detrimental consequences for the healing environment of the tendon. Abnormal stress can induce remodeling of the extracellular matrix and may lead to tendinopathies.^{38,39} High stress regions correlate with acellular regions,^{22,23} which is undesirable, as tenocytes (tendon cells) maintain tissue homeostasis. High stress observed in our FE model adjacent to the barbed suture may be the mechanism for barbed suture loosening, which has been reported in clinical studies.⁴⁰ In the FE analysis of the present study, only low loads have been applied, as the tendon description is valid for low strains.²² It is possible that at higher loads, the stress distribution may change and become more even across the barbs and throughout the tendon tissue.

The present study assumes a transversely isotropic, linear elastic behavior of tendon tissue, which is appropriate for low strains.²² A constitutive material description of tendon valid for higher strains would require accounting for the hyperelastic and viscoelastic behaviors of the tendon as opposed to using a linear elastic assumption. Such a behavior has been mathematically described in the literature^{41,42} and could be implemented within the tendon FE model. Furthermore, including additional levels of tendon hierarchy in the multiscale material model, such as tendon fascicles, would provide a closer approximation to the behavior of tendon tissue. This was beyond the scope of the present study; however, it is recommended for future development of this work to consider whether stress is more evenly distributed throughout the suture and tendon at high loads.

In previous studies, the failure of suture barbs was reported to occur either by barb bending or peeling from the suture shaft.²⁷ From the $X\mu$ CT results of the large displacement study (sample 1), we observe only two barbs bending, and no barbs peeling (Section 3.2) and a pattern was not observed between barb position and bending profile (Figure 7). The differing suture geometry in the present and previous studies may be responsible for the different barb failure mechanisms observed between this work and the work of Ingle et al. In the present study, a relatively large PDO suture was used (size 2, 0.6 mm in diameter) to ensure that the barbs could be identified from the $X\mu$ CT reconstruction; however, the suture used by Ingle et al. was a smaller (size 0, 0.4 mm in diameter) polypropylene (PP) suture.²⁷ Although Young's modulus of PDO and PP is similar,⁴³ in the smaller suture, the barbs are thinner, and therefore more flexible, making them more likely to bend or peel. In addition, despite the encouraging results of our tissue

pull-out study (Figure 3j), the staining procedure may have affected the mechanical properties, and thus barb behavior, particularly considering the fact that PDO is a degradable polymer. Future $X\mu$ CT scanning of the barbed suture in tendon, using a variety of suture materials of different sizes, would provide insights into the different barb failure mechanisms of different sutures. Such information would aid the surgeon in suture selection for a given surgical procedure.

Although the FE analysis demonstrates that all barbs located within the tendon tissue undergo some stress as the suture is withdrawn (Section 3.3), indicating that they all engage with the tissue, it is curious that only three barbs exhibit bending or peeling. We therefore hypothesize that a third failure mechanism may be responsible for barb failure in the remaining nine barbs, that is, the tendon tissue tears, resulting in the dislodgement of the barb; which would be comparable to a pull-out failure in a conventional tendon repair. The development of the FE model to simulate the application of higher loads across the barbed suture repair (as discussed previously) would allow investigation into whether tendon failure stress is reached in the tissue surrounding the barbs, which would indicate tissue tearing.

Although it is commonplace to use one replicate during $X\mu$ CT studies, we must take into consideration the potential for variability when interpreting the data from the $X\mu$ CT and FE studies, as the FE model was developed from one sample. During tensile testing of the barbed suture pull-out from tendon (Figure 6), a large variability between samples was observed in the force–displacement curves. This variability may have been caused by several potential reasons, such as variations between tissue samples or differing numbers of barbs engaging with the tissue. Furthermore, the mechanical response may differ in vivo, with the presence of cyclic loading and blood flow. Additionally, suture thickness and arrangement would differ from this study should barbed suture be used clinically for tendon repair. The suture pull-out tests (Figure 6) demonstrate that a 2 mm gap (considered clinically as a repair failure) would occur at low loads. Typically, 4–0 sutures would be used clinically, in a looping arrangement,¹⁷ which may indeed provide a more even distribution of stress throughout the tissues. A larger suture was appropriate in this study to enable $X\mu$ CT imaging of the barbs, and a simplified arrangement enabled the consideration of stress distribution along a length of barbed suture. FE modeling of the looping arrangements with a thinner grade of suture is recommended for future work to identify stress distribution in barbed suture arrangements which are currently being considered for clinical use.

Air-filled pores were observed from the $X\mu$ CT scans of both samples and were located only around the suture strand. These pores are not noted previously in the literature. We hypothesize that the pores would also arise in a surgical setting and could potentially be minimized by performing the procedure in a more hydrated environment. FE analysis confirms that the barbs which are located within a pore do not fully engage with the tendon tissue (Figure 8d); yet, if the pore is removed from analysis, a greater barb engagement is observed (Figure 8e). Minimizing the formation of the pores is therefore desirable to improve the barbed suture attachment to the tissue and increase the resultant repair strength. We hypothesize that the pores arise because of tissue damage during suture insertion. However, we are unable to determine why the pores occur, which could be due to the needle size or

type, the suture diameter, material, or type (barbed, monofilament, or braided). This could be studied using $X\mu$ CT imaging, comparing the suture damage from various needles, sutures, and in different tissues. The results of such a study would have a clear application in the development of barbed suture products for improved tissue attachment.

Although the displacements of the barbs in the 0.5 mm suture withdrawal $X\mu$ CT scan and FE simulation do not agree exactly (Figure 9), the moderate agreement between barb bending in the $X\mu$ CT and FE results which we observed here was regarded as acceptable for the verification of this FE model. This is because we were not concerned with the absolute values from the model, such as exact values of barb bending, or the exact values of stress. Rather, we were interested in more general, qualitative, information provided by the FE results, such as whether a given barb was exhibiting peeling or not and which areas of the tendon exhibited higher or lower stress.

5. CONCLUSIONS

The use of an $X\mu$ CT-informed and validated FE model in this case study has revealed the micromechanical stress response in a sutured tendon under force application. The technique was made possible because of the customized I₂KI–PBS staining method, which improved imaging contrast while minimizing mechanical and morphological tissue changes. Several previously unknown findings have been revealed using this novel approach, including the uneven distribution of stress through the suture and tendon and the observation and effect of pores surrounding the suture. This case study showcases the dramatic potential of the $X\mu$ CT-informed FE analysis on the study of implantable biomaterials for soft tissue applications. The technique can be readily translated for the study of other implantable devices and for other soft tissues, and we have discussed an approach toward adapting this method for other applications.

AUTHOR INFORMATION

Corresponding Author

*E-mail: sarah.cartmell@manchester.ac.uk.

ORCID

Shelley D. Rawson: 0000-0002-9407-4072

Author Contributions

The manuscript was written through contributions of all authors. All authors have given approval to the final version of the manuscript.

Notes

The authors declare no competing financial interest.

ACKNOWLEDGMENTS

This work was supported by the Engineering and Physical Sciences Research Council (grant numbers 1233537 and EP/L017997/1) and the Medical Research Council (MRC:G1000788/1). We are thankful to the staff at the Henry Mosley X-ray Imaging Facility at the University of Manchester for providing $X\mu$ CT scanning time and technical support.

ABBREVIATIONS

$X\mu$ CT, X-ray microcomputed tomography; FE, finite element; TE, tissue engineering; I₂KI, Iodine potassium iodide; FDP, *flexor digitorum profundus*; RT, room temperature; I₂KI–

dH₂O, iodine potassium iodide solution in distilled water; I₂KI–PBS, iodine potassium iodide solution in Dulbecco's phosphate-buffered saline (without Ca²⁺ or Mg²⁺); PDO, polydioxanone; PP, polypropylene

REFERENCES

- (1) Shearer, T.; Bradley, R. S.; Hidalgo-Bastida, L. A.; Sherratt, M. J.; Cartmell, S. H. Three-dimensional Visualisation of Soft Biological Structures by X-ray Computed Micro-Tomography. *J. Cell Sci.* **2016**, *129*, 2483–2492.
- (2) Johnson, J. T.; Hansen, M. S.; Wu, I.; Healy, L. J.; Johnson, C. R.; Jones, G. M.; Capecchi, M. R.; Keller, C. Virtual Histology of Transgenic Mouse Embryos for High-Throughput Phenotyping. *PLoS Genet.* **2006**, *2*, e61.
- (3) Metscher, B. D. MicroCT for Comparative Morphology: Simple Staining Methods Allow High-Contrast 3D Imaging of Diverse Non-Mineralized Animal Tissues. *BMC Physiol.* **2009**, *9*, 11.
- (4) Momose, A.; Fukuda, J. Phase-contrast radiographs of non-stained rat cerebellar specimen. *Med. Phys.* **1995**, *22*, 375–379.
- (5) Olivo, A.; Speller, R. Modelling of a Novel X-ray Phase Contrast Imaging Technique Based on Coded Apertures. *Phys. Med. Biol.* **2007**, *52*, 6555–6573.
- (6) Zeiss 3D X-ray Microscopes (XRM) for Scientific and Industrial Research. <https://www.zeiss.com/microscopy/int/products/x-ray-microscopy.html> (accessed Jan 5, 2018).
- (7) Mei, M. L.; Ito, L.; Cao, Y.; Lo, E. C. M.; Li, Q. L.; Chu, C. H. An ex vivo Study of Arrested Primary Teeth Caries with Silver Diamine Fluoride Therapy. *J. Dent.* **2014**, *42*, 395–402.
- (8) Effendy, N.; Khamis, M.; Shuid, A. Micro-CT Assessments of Potential Anti-Osteoporotic Agents. *Curr. Drug Targets* **2013**, *14*, 1542–1551.
- (9) Levrero-Florencio, F.; Margetts, L.; Sales, E.; Xie, S.; Manda, K.; Pankaj, P. Evaluating the Macroscopic Yield Behaviour of Trabecular Bone Using a Nonlinear Homogenisation Approach. *J. Mech. Behav. Biomed. Mater.* **2016**, *61*, 384–396.
- (10) Mustansar, Z.; McDonald, S. A.; Sellers, W. I.; Manning, P. L.; Lowe, T.; Withers, P. J.; Margetts, L. A Study of the Progression of Damage in an Axially Loaded Branta leucopsis Femur using X-ray Computed Tomography and Digital Image Correlation. *PeerJ* **2017**, *5*, e3416.
- (11) Bosworth, L. A.; Alam, N.; Wong, J. K.; Downes, S. Investigation of 2D and 3D Electrospun Scaffolds Intended for Tendon Repair. *J. Mater. Sci.: Mater. Med.* **2013**, *24*, 1605–1614.
- (12) Lima, M. J.; Corrello, V. M.; Reis, R. L. Micro/Nano Replication and 3D Assembling Techniques for Scaffold Fabrication. *Mater. Sci. Eng., C* **2014**, *42*, 615–621.
- (13) Lacroix, D.; Planell, J. A.; Prendergast, P. J. Computer-Aided Design and Finite-Element Modelling of Biomaterial Scaffolds for Bone Tissue Engineering. *Philos. Trans. R. Soc., A* **2009**, *367*, 1993–2009.
- (14) Winter, J. Hospital Episode Statistics, Admitted Patient Care—England, 2014–15: Procedures and Interventions. <http://www.hscic.gov.uk/> (accessed May 24, 2016).
- (15) Clayton, R. A. E.; Court-Brown, C. M. The Epidemiology of Musculoskeletal Tendinous and Ligamentous Injuries. *Injury* **2008**, *39*, 1338–1344.
- (16) Bunnell, S. Repair of Tendons in the Finger and Description of two new Instruments. *Surg., Gynecol. Obstet.* **1918**, *26*, 103–110.
- (17) Peltz, T. S.; Haddad, R.; Scougall, P. J.; Nicklin, S.; Gianoutsos, M. P.; Oliver, R.; Walsh, W. R. Structural Failure Mechanisms of Common Flexor Tendon Repairs. *Hand Surg.* **2015**, *20*, 369–379.
- (18) Rawson, S.; Cartmell, S.; Wong, J. Suture Techniques for Tendon Repair; a Comparative Review. *Muscles Ligaments Tendons J.* **2013**, *3*, 123–133.
- (19) Peltz, T. S.; Haddad, R.; Scougall, P. J.; Gianoutsos, M. P.; Bertollo, N.; Walsh, W. R. Performance of a Knotless Four-Strand Flexor Tendon Repair with a Unidirectional Barbed Suture Device: a Dynamic ex vivo Comparison. *J. Hand Surg.* **2014**, *39*, 30–39.
- (20) Wilkie, D. H. Elastic Barbed Suture and Tissue Support System. U.S. Patent 20,090,248,066, 2008.
- (21) Shah, A.; Rowlands, M.; Au, A. Barbed Sutures and Tendon Repair—a Review. *Hand* **2015**, *10*, 6–15.
- (22) Rawson, S. D.; Margetts, L.; Wong, J. K. F.; Cartmell, S. H. Sutured Tendon Repair; a Multi-Scale Finite Element Model. *Biomech. Model. Mechanobiol.* **2015**, *14*, 123–133.
- (23) Wong, J. K. F.; Alyouha, S.; Kadler, K. E.; Ferguson, M. W. J.; McGrouther, D. A. The Cell Biology of Suturing Tendons. *Matrix Biol.* **2010**, *29*, 525–536.
- (24) Su, B. W.; Protosaltis, T. S.; Koff, M. F.; Chang, K. P.; Strauch, R. J.; Crow, S. A.; Rosenwasser, M. P. The Biomechanical Analysis of a Tendon Fixation Device for Flexor Tendon Repair. *J. Hand Surg.* **2005**, *30*, 237–245.
- (25) Griffin, M.; Hindocha, S.; Jordan, D.; Sales, M.; Khan, W. An Overview of the Management of Flexor Tendon Injuries. *Open Orthop. J.* **2012**, *6*, 28–35.
- (26) Docheva, D.; Müller, S. A.; Majewski, M.; Evans, C. H. Biologics for tendon repair. *Adv. Drug Deliv. Rev.* **2015**, *84*, 222–239.
- (27) Ingle, N. P.; King, M. W.; Zikry, M. A. Finite element analysis of barbed sutures in skin and tendon tissues. *J. Biomech.* **2010**, *43*, 879–886.
- (28) Ingle, N. P.; King, M. W. Optimizing the tissue anchoring performance of barbed sutures in skin and tendon tissues. *J. Biomech.* **2010**, *43*, 302–309.
- (29) Ribi, W.; Senden, T. J.; Sakellariou, A.; Limaye, A.; Zhang, S. Imaging Honey Bee Brain Anatomy with Micro-X-Ray-Computed Tomography. *J. Neurosci. Methods* **2008**, *171*, 93–97.
- (30) Faraj, K. A.; Cuijpers, V. M. J. I.; Wismans, R. G.; Walboomers, X. F.; Jansen, J. A.; van Kuppevelt, T. H.; Daamen, W. F. Micro-Computed Tomographical Imaging of Soft Biological Materials using Contrast Techniques. *Tissue Eng., Part C* **2009**, *15*, 493–499.
- (31) Clavert, P.; Kempf, J.-F.; Bonnomet, F.; Boutemy, P.; Marcelin, L.; Kahn, J.-L. Effects of Freezing/Thawing on the Biomechanical Properties of Human Tendons. *Surg. Radiol. Anat.* **2001**, *23*, 259–262.
- (32) Shearer, T.; Rawson, S.; Castro, S. J.; Balint, R.; Bradley, R. S.; Lowe, T.; Vila-Comamala, J.; Lee, P. D.; Cartmell, S. H. X-ray Computed Tomography of the Anterior Cruciate Ligament and Patellar Tendon. *Muscles Ligaments Tendons J.* **2014**, *4*, 238–244.
- (33) Degenhardt, K.; Wright, A. C.; Horng, D.; Padmanabhan, A.; Epstein, J. A. Rapid 3D Phenotyping of Cardiovascular Development in Mouse Embryos by Micro-CT with Iodine Staining. *Circ.: Cardiovasc. Imag.* **2010**, *3*, 314–322.
- (34) Abe, M.; Takahashi, M.; Horiuchi, K.; Nagano, A. The Changes in Crosslink Contents in Tissues After Formalin Fixation. *Anal. Biochem.* **2003**, *318*, 118–123.
- (35) Havulinna, J.; Leppänen, O. V.; Järvinen, T. L. N.; Göransson, H. Comparison of Modified Kessler Tendon Suture at Different Levels in the Human Flexor Digitorum Profundus Tendon and Porcine Flexors and Porcine Extensors: an Experimental Biomechanical Study. *J. Hand Surg.* **2011**, *36*, 670–676.
- (36) Butters, T. D.; Castro, S. J.; Lowe, T.; Zhang, Y.; Lei, M.; Withers, P. J.; Zhang, H. Optimal Iodine Staining of Cardiac Tissue for X-ray Computed Tomography. *PLoS One* **2014**, *9*, e105552.
- (37) Balint, R.; Lowe, T.; Shearer, T. Optimal Contrast Agent Staining of Ligaments and Tendons for X-Ray Computed Tomography. *PLoS One* **2016**, *11*, e0153552.
- (38) Myer, C.; Fowler, J. R. Flexor Tendon Repair. *Orthop. Clin. N. Am.* **2016**, *47*, 219–226.
- (39) Screen, H. R. C.; Berk, D. E.; Kadler, K. E.; Ramirez, F.; Young, M. F. Tendon Functional Extracellular Matrix. *J. Orthop. Res.* **2015**, *33*, 793–799.
- (40) Atiyeh, B. S.; Dibo, S. A.; Costagliola, M.; Hayek, S. N. Barbed sutures “lunch time” lifting: evidence-based efficacy. *J. Cosmet. Dermatol.* **2010**, *9*, 132–141.
- (41) Shearer, T. A New Strain Energy Function for the Hyperelastic Modelling of Ligaments and Tendons Based on Fascicle Microstructure. *J. Biomech.* **2015**, *48*, 290–297.

(42) Puso, M. A.; Weiss, J. A. Finite Element Implementation of Anisotropic Quasi-Linear Viscoelasticity Using a Discrete Spectrum Approximation. *J. Biomech. Eng.* **1998**, *120*, 62–70.

(43) Greenwald, D.; Shumway, S.; Albear, P.; Gottlieb, L. Mechanical Comparison of 10 Suture Materials Before and After in vivo Incubation. *J. Surg. Res.* **1994**, *56*, 372–377.